Contents lists available at ScienceDirect

Neuroscience Informatics

www.elsevier.com/locate/neuri

Original article

Integrating anisotropic filtering, level set methods and convolutional neural networks for fully automatic segmentation of brain tumors in magnetic resonance imaging

Mohammad Dweik [a], Roberto Ferretti [b],*

[a] Department of Basic and Applied Sciences for Engineering (SBAI), Sapienza University of Rome, Via Antonio Scarpa, 14, Rome 00161, Italy
[b] Department of Mathematics and Physics, Roma Tre University, Largo San Leonardo Murialdo, 1, Rome 00146, Italy

ABSTRACT

An accurate, fully automatic detection and segmentation technique for brain tumors in magnetic resonance images (MRI) is introduced. The approach basically combines geometric active contours segmentation with a deep learning-based initialization. As a pre-processing step, an anisotropic filter is used to smooth the image; afterwards, the segmentation process takes place in two phases: the first one is based on the concept of transfer learning, where a pre-trained convolutional neural network coupled with a detector is fine-tuned using a training set of 388 T1-weighted contrast enhanced MRI images that contain a brain tumor (Meningioma); this trained network is able to automatically detect the location of the tumor by generating a bounding box with certain coordinates. The second phase takes place by using the coordinates of the bounding box to initialize the geometric active contour that iteratively evolves towards the tumor's boundaries. While most of the ingredients of this processing chain are more or less well known, the main contribution of this work is in integrating the various techniques in a novel and hopefully clever form, which could take the best of both geometric segmentation algorithms and neural networks, with a relatively light training phase. The performance of such a processing network is evaluated using a separate testing set of 97 MRI images containing the same type of brain tumor. The technique proves to be remarkably effective, with a precision of 97.92%, recall of 96.91%, F-measure of 97.41% and an average Dice similarity coefficient (DSC) for segmented images above 0.95.

© 2022 The Author(s). Published by Elsevier Masson SAS. This is an open access article under the CC BY-NC-ND license (http://creativecommons.org/licenses/by-nc-nd/4.0/).

1. Introduction

In medical imaging, an accurate detection and segmentation process for tumors plays an important role in their treatment. In particular, information such as the exact location and boundaries of the tumor, as well as its geometric parameters, could be extremely valuable for doctors in pre- and post-treatment procedures, surgical planning, and evaluation of a chemotherapy. This paper addresses itself to the detection and segmentation for some kinds of brain tumors.

Tumors are currently classified according to the 2021 Edition of the WHO Classification of Tumors. Primary brain tumors (i.e., brain tumors not resulting from metastases) may be grouped in various categories (see WHO Classification of Tumours Editorial Board [50]), the most frequent among which are gliomas and meningiomas. This work will concentrate on the specific case of meningiomas, which represent about 15-20% of the total number of brain tumors, and which present a benign evolution (i.e., do not tend to invade normal tissues) in more that 90% of the cases. Clearly, the methodology under consideration will be tuned on this particular case, but it relies on concepts that are applicable in other and more general situations.

Manual segmentation of tumors in MRI images usually takes place by marking the borders of the target object (tumor) or by painting it with a brush; this method is tedious, time consuming and highly operator-dependent, and this motivates the search for automatic algorithms to speed up the process and make it more reproducible. Several segmentation algorithms and different mathematical approaches have been developed in this field in the last decades: among others, thresholding [28,16], k-mean clustering [4], histograms-based methods [33], graph partitioning [17], region growing [1], and the wide range of level set methods [35,45,34]. In what follows, the focus will be on level set methods; two extensive reviews about their use in medical imaging are provided in Angelini et al. [3] and He et al. [21].
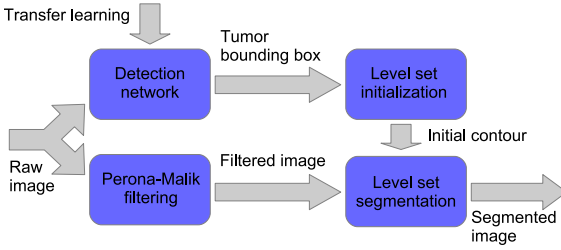
Fig. 1. Flow of the information in the processing chain proposed.

The common ingredient of these methods is to work on the basis of geometric features of the image: typically, sharp transitions in the gray level of the various regions. This fixes *a priori* the segmentation criterion. On the other hand, in more recent times, segmentation via machine learning techniques has gained a considerable popularity. In this case, the segmentation criterion results from a learning process, and may be different according to the training situations chosen; this feature makes machine learning techniques well suited for specific tasks in medical imaging, like detecting a tumor. Among the extensive literature on the topic, the reader is referred to Guo et al. [18] for general segmentation problems, and Nadeem et al. [31], Hashemzehi et al. [19], Bhandari et al. [6], Rehman et al. [40], Chattopadhyay and Maitra [12], Praveenkumar and Nagaraj [37] for the specific case of brain tumors.

This versatility of machine learning algorithms, however, comes at the price of a higher demand of both computing resources and learning data, for a sufficiently long training phase. In this work, some form of integrations between these two classes of techniques for tumor detection and segmentation will be pursued, in the attempt to reduce the training requirements, following the flowchart in Fig. 1:

- In an initial phase, a nonlinear filter is applied to smooth out the image and reduce noise and artifacts (which might cause a misbehavior of the segmentation algorithm), while enhancing the edges among internal regions. A classical choice for this task is an anisotropic filter of *Perona–Malik* type [36], which will be used as a pre-processing step.
- The following phase of segmentation will make use of the *geometric active contours* technique of Caselles et al. [9], which is based on a level set formulation (see Osher and Sethian [35]), and needs therefore to be initialized with an initial level set function (i.e., an initial contour), reasonably close to the target object – the tumor, in this case. Such a model may be used in a semi-automatic (or interactive) segmentation, in which the doctor, via a suitable user interface, manually initializes the contour around the object he or she detects as a tumor; then, the evolution of the contour under the PDE will take over and handle the rest of the segmentation process. While more reproducible than a completely manual segmentation, this approach remains nevertheless time-consuming and impractical in case of large amounts of images to be processed.
- In order to speed up the process, and avoid as much as possible any intervention by doctors, the initialization of the contour will be automated via a pre-trained neural network using the artificial intelligence technique known as *transfer learning*; this might be seen as a tumor detection phase, in which the detector generates a bounding box around the location of the tumor as a preliminary to the geometric active contour step. Since this kind of information is typically looser than a complete segmentation, an easier and faster training might be expected, as well as lower requirements in terms of computing resources.

- Using the bounding box provided by the detection network to initialize the contour of the level set segmentation requires some additional care. In what follows, an expanding level set model will be used to minimize the probability of a front collapse.

Some recent similar work has been done in using the deep learning as a preliminary step for level set segmentation. In the treatment of generic images, for instance, Kristiadi et al. [26], propose a detector to generate a bounding box to initialize the geodesic active contour algorithm, and Tang et al. [49] use the Chan–Vese active contour segmentation [11] to refine the output of a Fully Convolutional Network (FCN), this resulting in a semi-supervised learning procedure. In the processing of biomedical images, Ngo and Carneiro [32] couple a Deep Belief Network (DBN) with shape priors to initialize the active contour for left ventricle segmentation from cardiac MRI; Cha et al. [10] use a Convolutional Neural Network (CNN) to generate a likelihood map of proposed regions inside a bladder by using thresholding and hole filling, and initialize the active contour accordingly. Finally, it is worth mentioning the works done in Qin et al. [38], in which a deep neural network (DNN) is trained to classify center pixel of the image patches according to four MRI modalities (T1, T1ce, T2 and flair) and then use this pixel segmentation result as prior for a level set segmentation, and in Rehman et al. [41], using again the Chan–Vese segmentation to refine the output of a U-net in order to detect osteoporotic fractures of vertebrae.

The setting of the present work, and in particular the choice of a transfer learning approach, as well as the presence of a filtering phase and the active contour model chosen, combines the basic ingredients in a novel form. This paper describes this procedure in detail and provides numerical tests on a suitable benchmark, showing the effectiveness of the technique. Note that the entire procedure proposed may be implemented with 3D data and output, although this extension will not be pursued here.

The remaining part of the paper is organized as follows: Section 2 introduces the Perona–Malik filter used as a pre-processing step; Section 3 details the geometric active contour models proposed, Section 4 is concerned with the deep learning technique as a preliminary step for segmentation, and Section 5 discusses the numerical results of the complete processing chain. Lastly, the conclusion section summarizes the results and clarifies authors' contribution.

2. Perona–Malik filter

Perona–Malik filter is a nonlinear, anisotropic PDE-based filtering technique; this filter is conceived to locally smooth the small variations of the gray level of the image (considered as noise) and preserve the large ones (considered as edges).

The filter is formulated as follows: let $\Omega \subset \mathbb{R}^2$ denote a smooth bounded subset, typically a rectangle (a 3D version is also possible), and $I(x, y, t): \Omega \to \mathbb{R}$ a family of gray-scale images, then the Perona–Malik filtering is defined by the following initial-boundary value problem:

$$\begin{cases} \dfrac{\partial I}{\partial t} = \operatorname{div}\big(c\left(|\nabla I|\right) \nabla I\big) & (x, y, t) \in \Omega \times (0, T], \\ I(x, y, 0) = I_0(x, y) & (x, y) \in \Omega, \\ \dfrac{\partial I}{\partial \mathbf{n}} = 0 & (x, y, t) \in \partial\Omega \times (0, T]. \end{cases} \tag{1}$$

Here, the initial condition $I_0(x, y)$ is the original noisy image, $\mathbf{n}$ denotes the outward unit normal, $|\cdot|$ stands for the Euclidean norm, and the Neumann boundary conditions on $\partial\Omega$ are used to reduce as much as possible the effect of the boundary on the image.

Among the various structures proposed for the diffusion coefficient c, the form

$$c\left(|\nabla I|\right) = \frac{1}{1 + \left(\frac{|\nabla I|}{\lambda}\right)^2} \qquad (2)$$

will be permanently used in what follows. The diffusion coefficient $c: \mathbb{R}^+ \to \mathbb{R}^+$ is a strictly decreasing function that works as an edge-detector, in which $|\nabla I|$ is a measure of the edge strength; it satisfies $c\left(|\nabla I|\right) \to 0$ as $|\nabla I| \to \infty$, so that high values of $|\nabla I|$ (sharp edges) will decrease the diffusion, and accordingly preserve the edges from being blurred. On the other hand, the parameter $\lambda > 0$ controls the sensitivity to the strength of edges; it is experimentally tuned to be directly proportional to the noise level in the image. It might be regarded as a contrast parameter that separates the smoothing area from the sharpening area for a certain edge strength, so that, roughly speaking, the edges will be smoothed where $|\nabla I| < \lambda$ and will be sharpened where $|\nabla I| > \lambda$. This is related to a backward diffusion effect (see Kichenassamy [25]), and will improve the performance of the segmentation phase.

2.1. Numerical discretization scheme

Following the numerical discretization proposed by Gerig et al. [15], denote by $I_{i,j}^n$ the gray level of the pixel (i, j) at the time level n, and by respectively $I_N, I_{NE}, I_E, I_{SE}, I_S, I_{SW}, I_W, I_{NW}$ the north, nort-east, east, south-east, south, south-west, west and north-west finite differences of the pixel gray intensity at the n-th time level (setting conventionally the space step as $\Delta x = \Delta y = 1$), and C_i, $(i = N, NE, E, SE, S, SW, W, NW)$ the corresponding diffusion coefficient, so that for example

$$I_N = I_{i,j+1}^n - I_{i,j}^n, \qquad C_N = \frac{1}{1 + (I_N/\lambda)^2}, \qquad (3)$$

$$I_{NE} = I_{i+1,j+1}^n - I_{i,j}^n, \qquad C_{NE} = \frac{1}{1 + (I_{NE}/\lambda)^2}. \qquad (4)$$

Then, the scheme of Gerig et al. [15] reads

$$I_{i,j}^{n+1} = I_{i,j}^n + \Delta t \left(C_E I_E + C_W I_W + C_N I_N + C_S I_S \right) \qquad (5)$$
$$+ \frac{\Delta t}{2} \left(C_{NE} I_{NE} + C_{NW} I_{NW} + C_{SE} I_{SE} + C_{SW} I_{SW} \right),$$

where Δt is the time step. Finally, Neumann boundary conditions are handled via an extra frame of grid points (known as *ghost points*) outside the domain Ω. An analysis based on monotonicity provides for the scheme (5) the stability condition

$$\Delta t \leq \frac{1}{6}. \qquad (6)$$

2.2. Contrast parameter

In the simplest situation, the contrast parameter λ might be chosen experimentally according to the specific application, and kept fixed during the iterations; in this case, a criterion to stop the evolution of the filter (for example, the one proposed in Capuzzo-Dolcetta and Ferretti [8]) is also needed. This work will use instead a method based on the gradient norm distribution, and partially inspired by Canny [7]. Here, the contrast parameter will be updated at each iteration, and, rather than setting a suitable stopping time, a (nearly) stationary state of the filtered image will be reached.

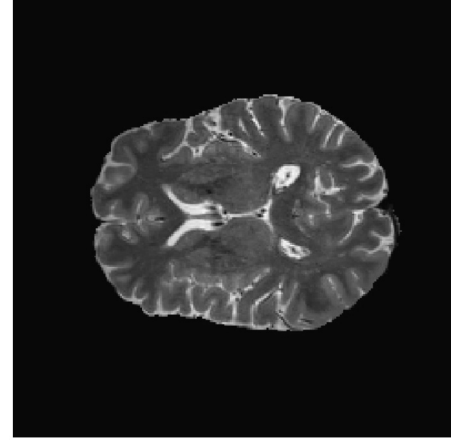First, the norm of the gradient of I is computed at each pixel using centered differences, as

Fig. 2. Axial MRI image of a human brain.

$$|\nabla I|_{i,j} = \sqrt{\left(\frac{I_N - I_S}{2}\right)^2 + \left(\frac{I_E - I_W}{2}\right)^2}. \qquad (7)$$

Then, the values are stored in a vector of size nm (where n and m represent the length and the width of the image), and the vector is sorted in ascending order, to draw the gradient norm distribution; this discrete sequence provides a good indication about the noise level in the image.

Fig. 2 shows a noisy 240×240 MRI image of a human brain, and Fig. 3 (top) its gradient norm distribution. The size of the vector is $240 \cdot 240 = 57600$ with a maximum value of 0.516 for the gradient norm.

The method suggests that the noise energy more likely comes from lower values of the gradient norm, while high values represent significant edges. Then, depending on the kind of image, the value of the contrast parameter λ might be set within the range 80th to 90th percentile of the sorted distribution, with higher values for more noisy images. In the case under consideration, λ is set at the 85th percentile, which corresponds to a value $\lambda = 0.035$; the annotated abscissa on Fig. 3 (top) represents the number of pixels in the image (85% of all pixels) that have a gradient norm less than or equal to the annotated ordinate (0.035). Now, in terms of Perona–Malik filtering, this means that regions of the image with gradient norms below this threshold will be smoothed, while regions above the threshold will be sharpened.

Then, the contrast parameter λ is updated at each time iteration to remain at the same percentile (85th, in this case) of the new gradient norm distribution, which evolves as shown in Fig. 3 (bottom). As a result of the increased smoothing of regions where the gradient has lower values, the sequence of values of λ is expected to decrease towards zero, as shown in Fig. 4. This naturally provides a stopping criterion in the form

$$\left| \frac{d\lambda(t)}{dt} \right| < \varepsilon, \qquad (8)$$

for a suitably small threshold ε.

Finally, the filtering results of the image in Fig. 2 are shown in Fig. 5; the iterative loop was cut off at iteration number 150, according to the threshold of interest, with good results. In this test, the time step was kept at its maximum ($\Delta t = 1/6$).

3. Geometric active contours

Segmentation will be performed here by means of the level set technique known as *geometric active contours*.

Geometric (or *geodesic*) active contours are deformable models proposed originally by Caselles et al. [9] and derived from the clas-
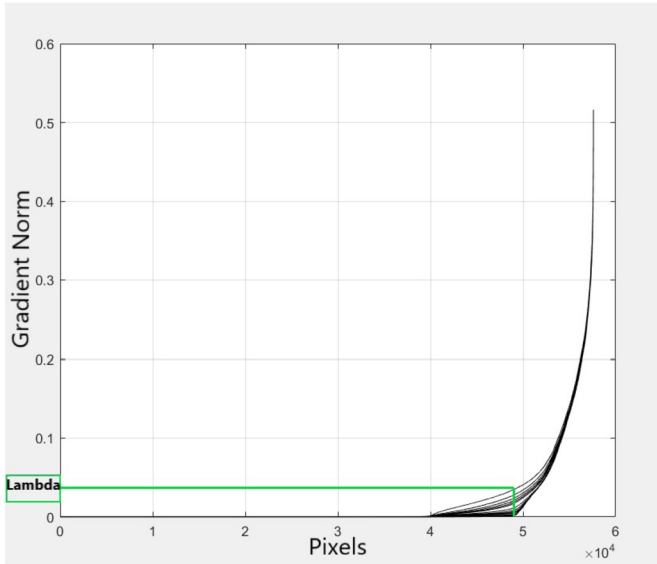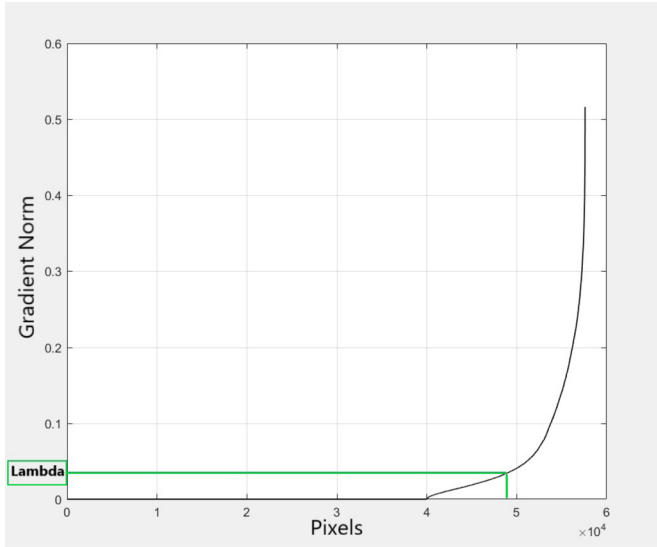
Fig. 3. Gradient norm distribution of the noisy image (I_0) of Fig. 2 with its corresponding contrast parameter λ (top) and evolution of the gradient norm distribution over time (bottom).
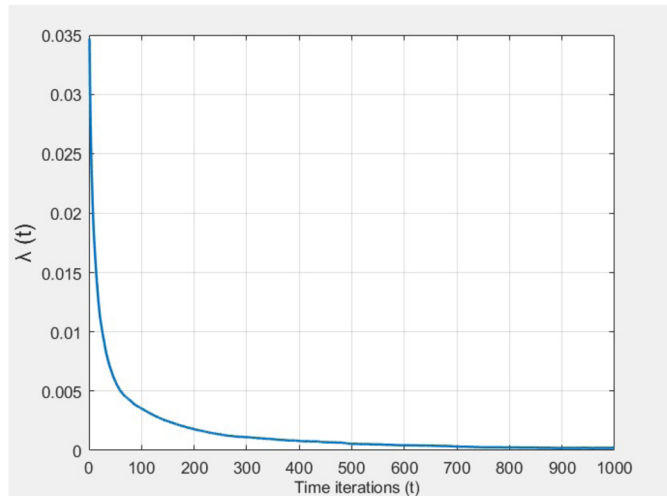

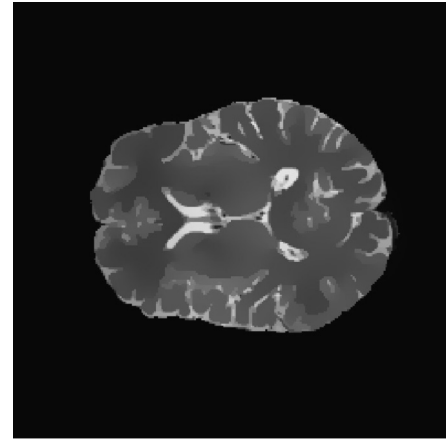**Fig. 4.** The contrast parameter as a function of time iterations.

Fig. 5. Anisotropic filtering results of the axial MRI image shown in Fig. 2, after 150 iterations.

sical energy functional-based model (snakes) by Kass et al. [24], in the framework of the level set method by Osher and Sethian [35].

The basic idea is that, once initialized the zero-level set (contour) close to the boundaries of an object in a certain image, the level set function starts evolving under a geometric time-dependent nonlinear partial differential equation, until it converges to a steady state solution; at this stage, the final zero-level set will be considered as the boundary of the object. In this paper, starting from the well-known model by Caselles et al. [9], a second model will be proposed to overcome some slight drawbacks of the first one.

3.1. Balloon model

The geometric active contour model proposed by Caselles et al. [9] is called the *balloon model*, and takes the form

$$\varphi_t = g\left(\nabla \hat{I}\right) \text{div} \left(\frac{\nabla \varphi}{|\nabla \varphi|}\right) |\nabla \varphi| + \nabla g\left(\nabla \hat{I}\right) \cdot \nabla \varphi + g\left(\nabla \hat{I}\right) |\nabla \varphi|,$$

(9)

where φ denotes the level set function, $\hat{I}$ is the smoothed image, and $g(\nabla \hat{I})$ is an *edge-detector function*, inversely related to the image gradient, defined as

$$g\left(\nabla \hat{I}\right) = \frac{1}{\alpha + \beta \left|\nabla \hat{I}\right|^p}.$$

(10)

Here, p is a parameter at the increase of which the function $g(\nabla \hat{I})$ becomes more sensitive to sharp edges ($|\nabla \hat{I}| > 1$) and less sensitive to weak edges ($|\nabla \hat{I}| < 1$); usually, $p \geq 1$. The parameters α and β are tuned in order to balance the speed of propagation of the front between edge and non-edge regions (typically, they can both be set as $\alpha = \beta = 1$), and affect the stability condition.

Under the effect of such an edge-detector function, higher gradients reduce the speed of the contour and vice versa, while the advection term $\nabla g \cdot \nabla \varphi$ "pushes" the level set towards the edge. The geometric interpretation of this latter effect is shown in Fig. 6 which shows a Sagittal MRI image of a human brain (top) where it is possible to notice the tumor and the vector field ∇g (bottom); a tiny part of the tumor boundaries has been magnified to better show the corresponding vector field. This effect is stronger after the edge enhancement operated by the Perona–Malik filter.
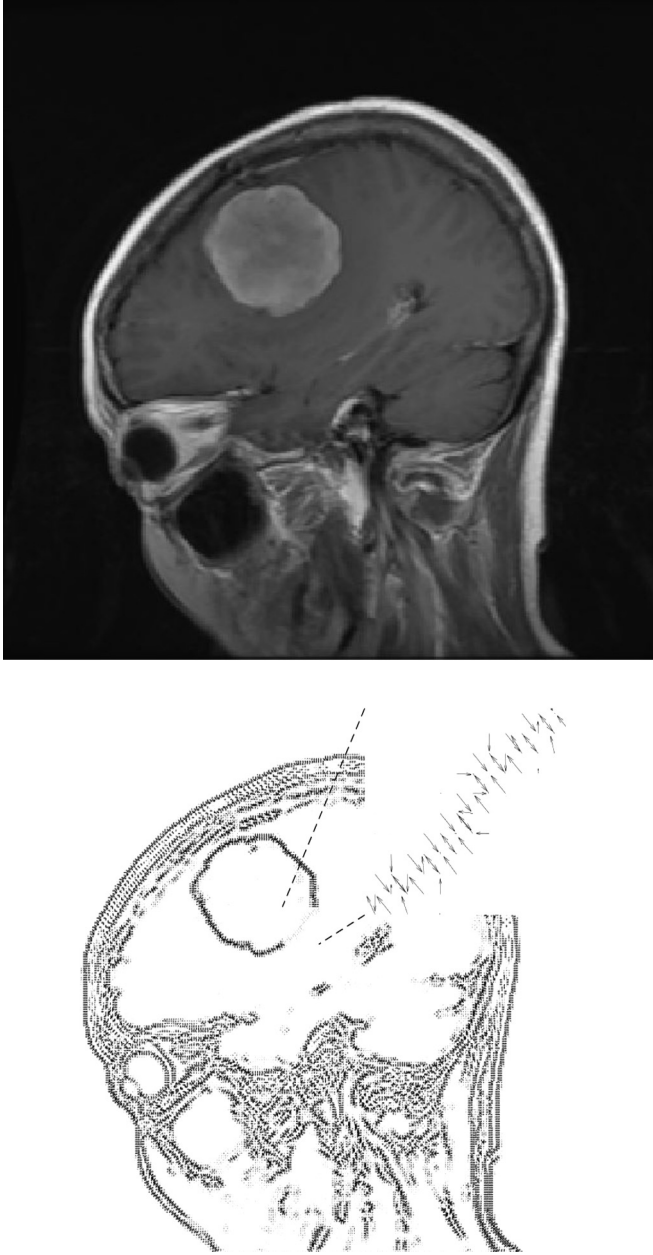
Fig. 6. A sagittal T1-weighted contrast enhanced MRI image of a brain tumor (top) and its vector field ∇g (bottom) with ($p = 4$).

3.2. Numerical method

The discretization of the various terms in (9) has been carried out along the following guidelines:

- For the edge-detector function at pixel (i, j), $g_{i,j}$, the gradient of $\hat{I}$ has been approximated via centered finite differences. A further application of centered finite differences on the values $g_{i,j}$ is used to approximate the gradient ∇g which appears in the transport term.
- The second-order (curvature) term in (9) is put in its explicit form

$$\text{div}\left(\frac{\nabla \varphi}{|\nabla \varphi|}\right) = \frac{\varphi_{xx}\varphi_y^2 - 2\varphi_x\varphi_y\varphi_{xy} + \varphi_{yy}\varphi_x^2}{\left(\varphi_x^2 + \varphi_y^2\right)^{3/2}}, \tag{11}$$

then all the terms are treated in centered form, in particular with the standard second difference for the terms φ_{xx} and φ_{yy}, and with the mixed difference

$$\varphi_{xy} \approx \frac{\varphi_{i+1,j+1} - \varphi_{i-1,j+1} - \varphi_{i+1,j-1} + \varphi_{i-1,j-1}}{4\Delta x \Delta y} \tag{12}$$

for the derivative φ_{xy}.

- The discretization of the term $|\nabla \varphi|$ is handled via an upwind monotone technique, proposed in Osher and Sethian [35] using ideas from hyperbolic conservation laws; it takes the form

$$|\nabla \varphi|_{i,j} = \left(\max\left(\frac{\varphi_{i+1,j} - \varphi_{i,j}}{\Delta x}, 0\right)^2 \right.$$
$$+ \min\left(\frac{\varphi_{i,j} - \varphi_{i-1,j}}{\Delta x},\right)^2 + \max\left(\frac{\varphi_{i,j+1} - \varphi_{i,j}}{\Delta y}, 0\right)^2$$
$$\left. + \min\left(\frac{\varphi_{i,j} - \varphi_{i,j-1}}{\Delta y}, 0\right)^2 \right)^{1/2}. \tag{13}$$

- Last, the term $\nabla g \cdot \nabla \varphi = g_x\varphi_x + g_y\varphi_y$ is also discretized in upwind monotone form as

$$(\nabla g \cdot \nabla \varphi)_{i,j} = \max\left(g_x, 0\right)\frac{\varphi_{i+i,j} - \varphi_{i,j}}{\Delta x}$$
$$+ \max\left(g_y, 0\right)\frac{\varphi_{i,j+1} - \varphi_{i,j}}{\Delta y} + \min\left(g_x, 0\right)\frac{\varphi_{i,j} - \varphi_{i-1,j}}{\Delta x}$$
$$+ \min\left(g_y, 0\right)\frac{\varphi_{i,j} - \varphi_{i,j-1}}{\Delta y}, \tag{14}$$

where the first derivatives of g, as already pointed out, are computed in centered form.

To be consistent with the discretization of the Perona–Malik model, set $\Delta x = \Delta y = 1$. Using an explicit Euler discretization of the time partial derivative with a time step Δt, this results in a stability condition of the form

$$\Delta t \leq \frac{1}{\max\left\{\left|g\left(\nabla\hat{I}\right)(k+1)\right| + \left|\nabla g\left(\nabla\hat{I}\right)\right|\right\}}, \tag{15}$$

which typically results in a somewhat restrictive bound on Δt.

3.3. Stopping criterion

In order to stop the evolution when sufficiently close to a stationary solution of (9), the stopping criterion adopted is based on the updates of the area enclosed by the zero-level set of φ, and more precisely

$$\left|\frac{\partial A_c(t)}{\partial t}\right| < \varepsilon, \tag{16}$$

where ε is a suitably small threshold, and $A_c(t)$ is the area enclosed at time t by the level curve, which, following Zhao et al. [52], is computed pixel-wise at each iteration as

$$A_c = \int_\Omega H\left(-\varphi(x, y)\right) dxdy, \tag{17}$$

where $H(x)$ is the Heaviside function given by

$$H(x) = \begin{cases} 1 & x \geq 0, \\ 0 & x < 0, \end{cases} \tag{18}$$

and the minus sign agrees with the conventional properties of the level set function $\varphi(x, y)$, which takes negative values inside the zero-level set and positive values elsewhere.

In order to avoid pseudo-convergence situations in which the front might be slowed down by some small obstruction, the iterations are stopped once the criterion (16) is satisfied for a certain number of consecutive iterations.

3.4. Inside-out model

The balloon model previously introduced presents a drawback when segmenting objects such as brain tumors in MRI images. In fact, the tumor is usually surrounded by other soft and uneven tissues; therefore, the evolving contour could be intercepted by their edges and fail to capture the exact tumor boundaries in lack of a very precise initialization. On the other hand, the region inside the tumor is typically more uniform, and this suggests the use of a model generating an expanding front.

This work proposes a model as such, which can be initialized entirely inside the object in a robust way. The model will be termed *inside-out model*, and has the form:

$$\varphi_t = \nabla g \left(\nabla \hat{I} \right) \cdot \nabla \varphi - g \left(\nabla \hat{I} \right) |\nabla \varphi|. \qquad (19)$$

As in the balloon model, the advection term $\nabla g \cdot \nabla \varphi$ forces the front towards the edge of the region, but, opposite to the balloon model, the eikonal term $g \left(\nabla \hat{I} \right) |\nabla \varphi|$ appears with the negative sign to generate an expanding front. In lack of a regularizing curvature term, the model is expected to be more sensitive to noise; however, this segmentation technique will only be applied after a previous regularization via the Perona–Malik filter.

As for the discretization of (19), the edge-detector function $g(\nabla \hat{I})$ is computed with centered differences as in the previous case; the discretization of the advective term $(\nabla g \cdot \nabla \varphi)$ is also identical to (14). On the other hand, due to the change in the sign of the eikonal term, all min/max operators of the upwind discretization described in (13) should be reversed. The stability condition for the scheme is easily obtained as

$$\Delta t \leq \frac{1}{\max \left\{ |g_x| + |g_y| \right\}}. \qquad (20)$$

In general, the lack of a curvature term leads to a less restrictive stability condition.

Finally, the stopping criterion (16) is also used for this model.

3.5. Numerical results

Figs. 7 to 10 display some results for a segmentation carried out with both level set models previously introduced. In addition to being easier to initialize, the inside-out model proves able to locate an internal hole in the region to be segmented, while the balloon model, based on a shrinking curve, is in turn able to segment a disconnected region. Note that the figures report the evolving front at successive times (starting from an elliptical initialization), and denser regions correspond to sectors in which the front has a slower evolution. The black curve denotes the final position of the front.

Balloon model Figs. 7 and 8 show two potentially critical situations. In the first one, the contour evolves to enter a non-convex region and achieve a complete segmentation of the tumor; the possibility of detecting non-convex boundaries is related to a sufficiently strong shrinking eikonal term. On the other hand, Fig. 8 shows a typical splitting of the front, operated by the level set approach to follow disconnected regions (a fragmented tumor). Again, the eikonal terms plays a crucial role in the topology change.
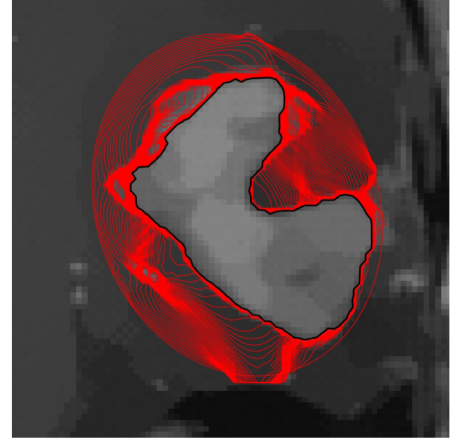

Fig. 7. A magnified balloon evolution of an initial contour around a brain tumor that contains a non-convex region.
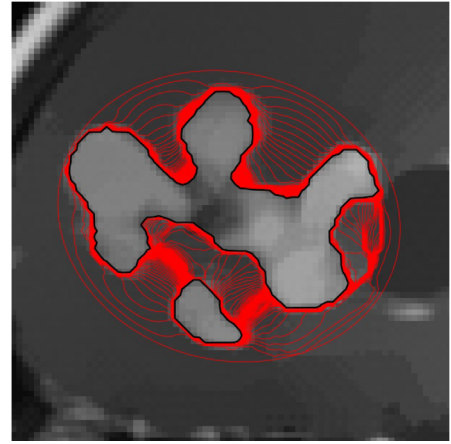

Fig. 8. A magnified balloon evolution of an initial contour around a fragmented brain tumor and its ability to split.
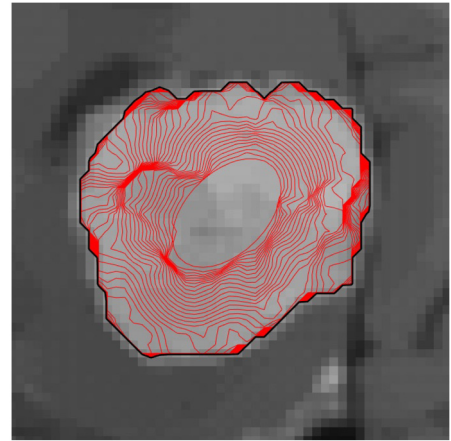

Fig. 9. A magnified inside-out evolution of an initial contour inside a tumor.

Inside-out model Fig. 9 reports the outward evolution of a contour initialized in the tumor under the inside-out model, while Fig. 10 shows that the inside-out model is capable of segmenting tumors with holes, via merging of different sections of the front.

As a final remark, it is worth to show how the Perona–Malik pre-processing makes it possible to successfully apply the inside-out model, which, in view of the lack of a regularization term,
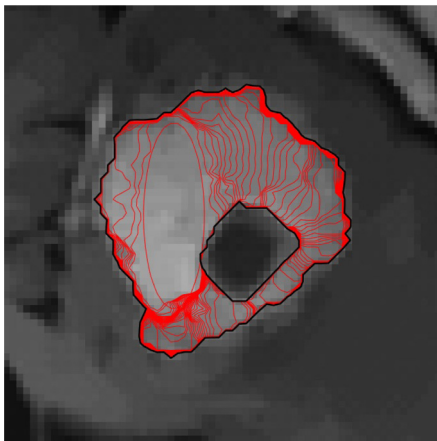
Fig. 10. A magnified inside-out evolution of an initial contour that captures a tumor with a hole.
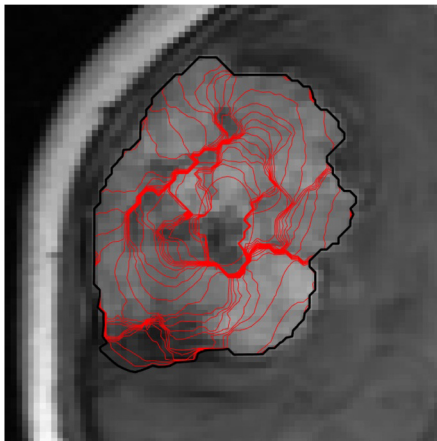

Fig. 11. A magnified inside-out model evolution of an initial contour inside a brain tumor (Meningioma) in raw T1-weighted contrast enhanced image.

Fig. 12. A magnified inside-out model evolution of an initial contour inside a brain tumor (Meningioma) in the same image shown in Fig. 11 but filtered using Perona-Malik filter with contrast parameter (λ) of 80th percentile.

Fig. 13. Structure of the transfer learning approach.

would be unsuitable in general to treat noisy images. In Fig. 11, the inside-out model is applied to an unfiltered image, and it can be noticed that the propagation of the contour is slower, and tends to be stuck in noisy regions. In addition, the model is unable to properly segment the tumor, since the weak edges at the bottom of the tumor are not sharp enough to stop the contour. In Fig. 12, the same test is performed after a Perona–Malik pre-processing, which results in a faster and more accurate detection. In fact, the filter not only smooths the image, but also sharpens the weak edges in the bottom region.

4. Deep learning

As mentioned above, the segmentation process pursued so far may be classified as *semi-automatic* or *interactive*: through a user-interface, the operator (radiologist or clinician) manually initializes the position of the contour around the object with a mouse click. Now, in order to fully automate the brain tumor detection without the need for the doctor's experience, initialization will be performed via the artificial intelligence techniques known as *deep learning*, while the subsequent segmentation phase will be taken over by one of the two models introduced and tested in the previous sections.

Deep learning is currently the cutting-edge in the field of machine learning; it is based on applying deep neural networks (DNNs) 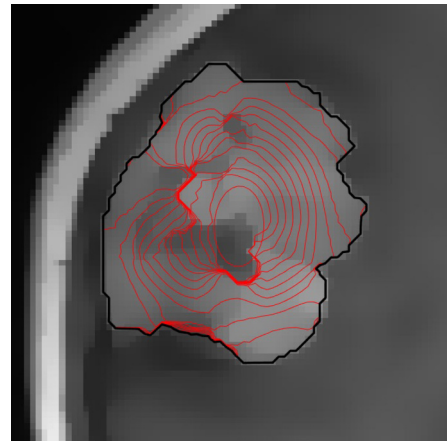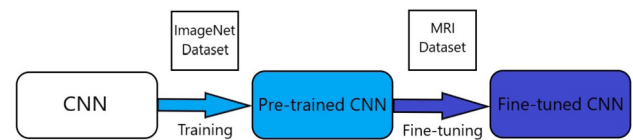that basically simulate the mechanism of biological neu-ral networks in the human brain, and its ability to learn. The word *deep* refers to multiple hidden layers (more than two), where the neural network learns hierarchical abstract representations of the data, one in each hidden layer; such networks have shown a high level performance that is close to human level in many areas, and in particular computer vision and medical diagnosis.

The task here is to automate a first, rough brain tumor detection in MRI images; to this end it is natural to make use of the deep neural networks specifically directed to patterns recognition in images, called *convolutional neural networks* (CNNs) or ConvNets, which basically mimic the visual cortex in the human brain and its capability to recognize patterns. In image segmentation, CNNs can in principle handle the entire segmentation process from end to end, which means that the ConvNet learns everything from input to output as a single complex task without any further steps, as in U-Nets (Ronneberger et al. [43]), which were developed specifically for biomedical image segmentation. Such networks are powerful and accurate, but computationally much more expensive than networks designed only for object detection, since they tend to be much deeper in terms of convolutional layers (Guo et al. [18]).

In general, properly training from scratch a deep ConvNet with high accuracy to detect the location of a tumor, and avoid overfitting, would require a large amount of MRI images – thousands or tens of thousands. In many situations, the reduced availability of labeled MRI images of brain tumors (only 485 meningioma images in the case under consideration) backs the use of another common technique in deep learning, known as *transfer learning*, which can overcome this data limitation.

4.1. Transfer learning

In the transfer learning approach, a deep CNN that has been already trained for a certain task is used as a starting point, after being re-tuned on a limited data set (MRI images in this case), as shown in Fig. 13. This process transfers the previous knowledge of the pre-trained network; in the case under consideration, this knowledge is basically the ability to recognize generic features of

objects in an image (e.g., lines, curves, corners or edges), and the deeper the network is, the more complex features it learns, which is a desirable point in medical diagnosis.

The majority of popular pre-trained networks, such as AlexNet (Krizhevsky et al. [27]), VGGNet (Simonyan and Zisserman [46]), GoogleNet (Szegedy et al. [48]) and ResNet (He et al. [20]) are image classification highly deep CNNs that have been trained on huge scale data sets database from ImageNet [23], which consists of more than a million images, and can classify them into 1000 object categories, such as animals, plants, scenery and so forth. Therefore, using these rich extracted features of the pre-trained networks as a backbone to train the first stage of the detection network will be much easier and faster than training it from scratch.

The following stage is an object detector that has two heads; one uses bounding box regression to localize the tumor using a bounding box with certain coordinates (regressor), and the second classifies and labels the detected tumor (classifier).

The most popular state-of-art object detectors are Faster-RCNN (Region-based CNNs) (Ren et al. [42]), YOLO (You Only Look Once) (Redmon et al. [39]) and SSD (Single Shot multibox Detector) (Liu et al. [29]). At a comparison, Faster-RCNN is relatively slower, but more accurate in the detection with respect to the other models (Sachan [44]), and this is the first motivation to adopt this network's architecture. The second motivation is that the size of some brain tumors is relatively small compared to the size of the image, and in this context, Faster-RCNN model has also an advantage over other models at detecting small objects (Hui [22]).

4.2. Faster-RCNN detector

Faster-RCNN is a network proposed by Ren et al. [42], whose general architecture is made up of Fast-RCNN coupled with a small convolutional network called region proposal network (RPN); this network learns how to predict region proposals to be extracted from the feature map of the pre-trained classification CNN.

Regarding the pre-trained network, it has been discussed in Zhang et al. [51], Hui [22], and Ma et al. [30] that the residual networks family (ResNet-18, ResNet-50, ResNet-101), together with InceptionResNet v2 (Szegedy et al. [47] perform the best as a backbone particularly for Faster-RCNN with respect to other pre-trained models mentioned earlier in terms of accuracy; ResNet family is developed by Microsoft Research Asia (He et al. [20]), and it has won ImageNet and COCO competitions in classification and detection. This work has been carried out with the limited computational resources of a laptop computer, and this supports the use of the network of least depth (ResNet-18), which is 18 layers deep. In fact, the other versions (50 and 101 layers deep) have an extremely expensive training which cannot be handled in reasonable time by a laptop due to low RAM memory and GPU capabilities.

ResNet-18 is a CNN with 11.7 million learnable parameters (weights and biases) and an input image size of 224×224 pixels, pre-trained on the database from ImageNet [23]; despite its relative simplicity, it is rich enough of generic features to be used in the detection network, following the general structure shown in Fig. 14.

4.3. Pre-processing and training

Meningioma MRI images are taken from a publicly shared database containing grayscale 16-bits unsigned integers T1-weighted contrast enhanced images (Cheng [13]), along with the exact location of each tumor as processed by doctors: in total, 485 meningioma images of three different planes, axial, sagittal and coronal. The images are partitioned into an 80% training set (388 images) and a 20% test set (97 images). All implementations, preprocessing, training and testing throughout this paper were carried out in
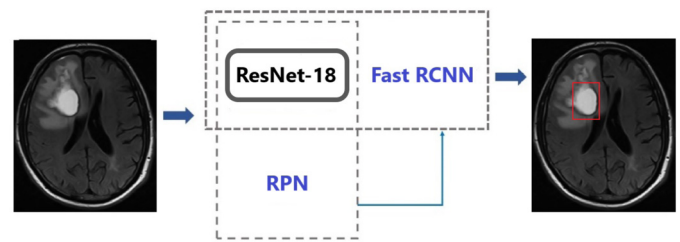

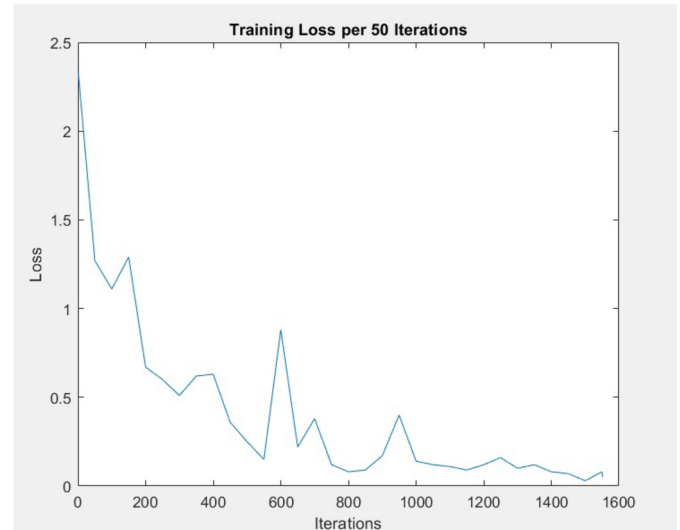**Fig. 14.** The general architecture of the detection network.

Fig. 15. The training loss of the model proposed.

MATLAB R2020b on a laptop with an Intel(R) Core(TM) i7-10710U CPU @ 1.10 GHZ 1.61 GHZ processor, 16.00 GB RAM and a Microsoft Windows 10 Home; in addition, a GPU NVIDIA GeForce GTX 1650 with Max-Q Design, a compute capability of 7.5 and total memory of 4295 MB. Since the detection network works in *supervised learning*, it needs ground-truth data obtained by manually labeling the training set image by image (388 images) using a bounding box that surrounds the tumor in accordance with the given doctors' indications using MATLAB application *Image Labeler*.

Next, the number of classes that are supposed to be the output of the classifier are defined; in this case only one class (meningioma) plus one extra class for background. Also, some *hyperparameters* are to be set before the training process: the first one is the *learning rate*, for which an empirical value of 0.001 has been adopted; the second one is the *momentum coefficient* $\beta = 0.9$ for the *stochastic gradient descent with momentum* (SGDM) optimization algorithm; the third one is the number of *epochs*, which was set to 8 epochs, since a higher number led to over-fitting; the last one is the *mini-batch size* which was set to 2.

In the end, it took 1 hour 17 mins to train the network through 1552 iterations in a total of 8 epochs, with 194 iterations per epoch, where this number equals the number of images in the training set divided by the mini-batch size. Finally, the training loss of the model over iterations is illustrated in Fig. 15, with a drop from 2.33 at the first iteration of the first epoch to 0.05 at the last iteration of the last epoch.

5. Testing and results

In the testing phase, the performance and accuracy of the trained detection network is evaluated using the 97 MRI images

testing set; here, the manually labeled ground-truth bounding boxes are compared with the bounding boxes generated by the network. The performance of the detector is assessed using specific metrics, in particular *recall*, *precision* and *F-measure*, defined as

$$\text{Recall} = \frac{TP}{TP + FN}, \tag{21}$$

$$\text{Precision} = \frac{TP}{TP + FP}, \tag{22}$$

$$\text{F} = 2\frac{\text{Precision} + \text{Recall}}{\text{Precision} \cdot \text{Recall}} = \frac{TP}{TP + \frac{1}{2}(FP + FN)}, \tag{23}$$

where TP, FP and FN are the numbers of respectively true positives, false positives and false negatives.

Dice similarity coefficient (DSC) will be used for the evaluation of the segmentation phase (see Crum et al. [14]). Given a ground truth segmentation G and an experimental segmentation S, this index is defined as

$$DSC = \frac{2|G \cap S|}{|G| + |S|}, \tag{24}$$

where $|A|$ denotes the measure of the set A (typically, the number of pixels). DSC is always in the range $[0, 1]$, with $DSC = 0$ indicating that G and S are disjoint sets, and $DSC = 1$ that $G = S$. In Matlab implementations, DSC can be computed via the built-in function `dice`.

5.1. Detection

Regarding the performance of the detector, the values of recall and precision were computed with respect to a value of *intersection over union* (IoU) of at least 0.5, i.e., the intersection between the labeled ground-truth bounding box and the detected bounding box over their union is at least 0.5. Accordingly, 94 images resulted as true positives, which means that the detection network has provided 94 bounding boxes that overlap with $IoU \geq 0.5$ with the ground-truth bounding boxes; two images turned out to be false positives, i.e., the network has provided bounding boxes that overlap with $IoU < 0.5$ with the ground-truth bounding boxes; finally, one image was a false negative, i.e., the network failed to detect a tumor and generate a bounding box, given an image actually containing a tumor. In the case of the two false positive results, there were no other boxes to correctly detect the tumor ($IoU \geq 0.5$) in the same image, so they can be also considered as false negatives (Aidouni [2]); thus, in total, 3 cases turned out to be false negatives.

Computing the metrics (21), (22) and (23), the detector has reached a recall of 96.91%, a precision of 97.92%, and an F-measure of 97.41%. These values seem to indicate a fairly good performance at detecting true positives boxes with respect to both the total positives boxes and all the ground-truth boxes.

In addition, the accuracy of the detection network has also been evaluated via the *average precision (AP)*, i.e., the average of all precisions across all recall values between 0 and 1 at a certain IoU threshold (0.5 in this case). Plotting the precision–recall curve as shown in Fig. 16, the average precision is computed as the *area under the curve (AUC)*, which also represent the integral mean of the precision. This metric evaluates the performance of the network with respect to both recall and precision; in this case, an average precision of 0.9684 (or 96.84%) has been obtained.

5.2. Segmentation

In the context of the image segmentation task described, the correctness of the final result does not only depend on the first
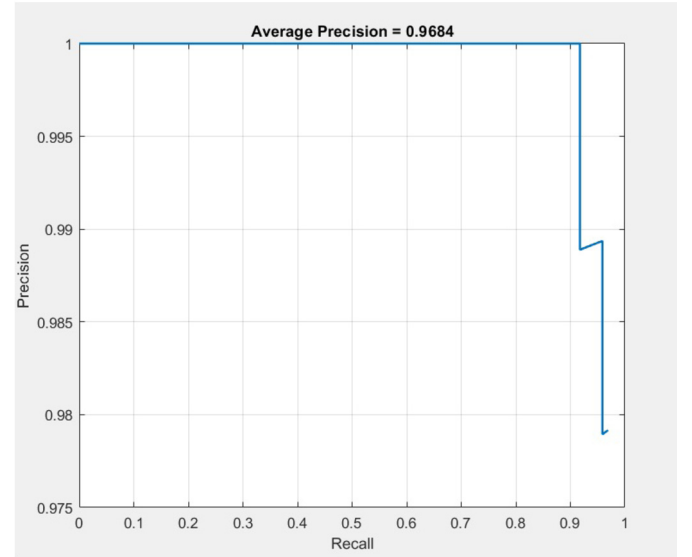

Fig. 16. Precision versus recall over the whole testing set with $IoU \geq 0.5$.

stage (detector), but also on the second stage (contour evolution); therefore, at this stage the evaluation will be performed via the DSC index defined in (24).

After detecting the tumor, the bounding box is described by the four values p_x, p_y, p_w, p_h, i.e., the center coordinates, the width and the height of the rectangular box. For the phase of level set segmentation, the natural initialization of the contour is an ellipse centered at (p_x, p_y); therefore, the level set function $\varphi(x, y)$ is initialized in the form

$$\varphi(x, y) = \left(\frac{x - p_x}{a}\right)^2 + \left(\frac{y - p_y}{b}\right)^2 - 1, \tag{25}$$

where a and b are the semi-axes in the x and y direction respectively.

In the case of the balloon model, the semi-axes have been assigned to be half of the width and the height of the detected bounding box ($a = p_h/2, b = p_w/2$), so that the ellipse touches the edges of the bounding box. In this first attempt, only 83 images over 97 have been successfully segmented; the main reason for the 13 failures (plus one FN) is that part of the initial contour was inside the tumor, and accordingly the contour has missed out the boundaries and has finally collapsed. In a similar way, initializing the contour to be a bit larger than the bounding box, the balloon model is also susceptible to miss out the correct segmentation because of possible obstacles surrounding the tumor.

On the other hand, the inside-out model proposed here has outperformed the balloon model; since in this case the semi-axis in the x and y direction is assigned to be one-sixth of the height ($a = p_h/6$) and width ($b = p_w/6$) of the bounding box respectively, this initial small elliptic contour is likely to be completely internal to the tumor region even for relatively small values of IoU: in particular, the value of $IoU \geq 0.5$ used to evaluate the detection phase may reasonably ensure that this condition is satisfied. Based on this initialization, all images were successfully segmented except for the false negative (96 images); and although $IoU \leq 0.5$ for 2 false positive images, these images have still been segmented, since they overlapped internally with the ground truth boxes. The evaluation of the DSC on the 96 successfully segmented images has provided values ranging in the interval $[0.931, 0.9833]$, with an average value of $DSC = 0.9605$.

Finally, Fig. 17 demonstrates the segmentation results of an automatically detected meningioma of a sagittal plane sample of the
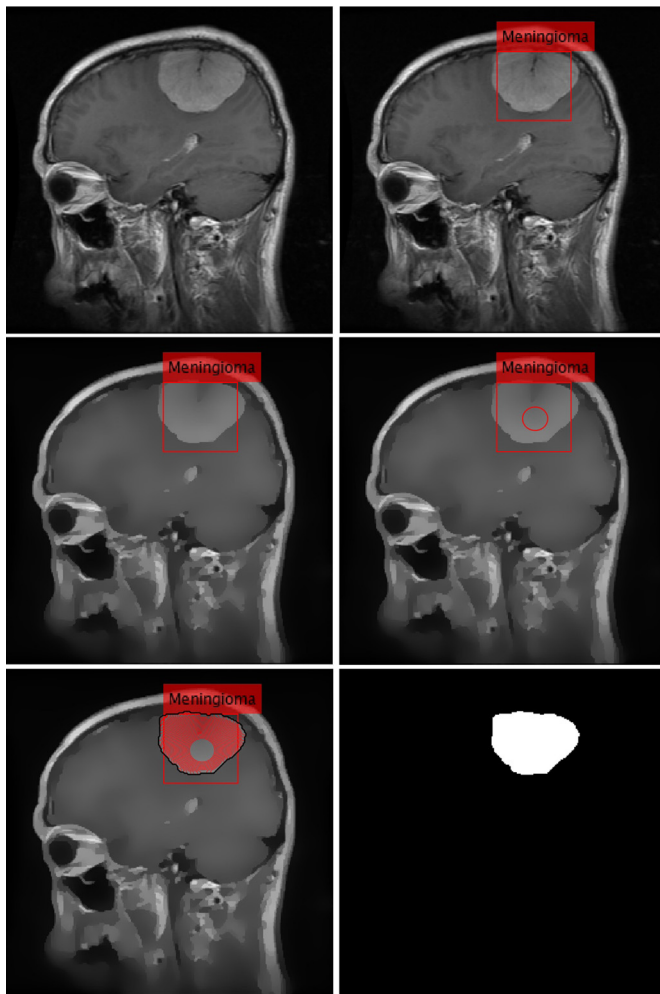
Fig. 17. Fully automatic segmentation results of one MRI image of the testing set using the processing chain proposed.

T1-weighted contrast enhanced MRI images testing set using the inside-out model. Fig. 17 top left shows the raw MRI image, top right the detected bounding box using the deep detection network proposed, mid-left the filtered image with contrast parameter of 80th percentile, mid-right the initial contour, bottom left the outward evolution of the contour until the tumor boundaries are located. Last, bottom right image shows the final binary segmentation ($\varphi(x, y) < 0$) of the tumor (mask), where the relevant geometric information can be extracted.

5.3. Processing times

As for the processing times, under Matlab and with the specific platform used, it takes about 0.4 s to detect a tumor in a single image via the bounding box. The filtering phase, as well as the segmentation phase, have a moderate dependence on the particular image processed, but are roughly in the range 5–10 s for filtering, and 10–20 s for segmentation via the inside-out model (slightly more for the balloon model, due to the stronger restrictions on the time step).

5.4. Comparison with different algorithms

At the current stage, a number of different methods based on Machine Learning have been proposed. Among the references, we quote some review paper evaluating different approaches and architectures to compare with.

- Concerning the detection phase:
  - Hashemzehi et al. [19] propose a hybrid CNN–NADE (neural autoregressive distribution estimation) network, and compare this network architecture versus different structures in the detection of meningiomas, gliomas and pituitary tumors, reporting values of the F-measure ranging up to about 95-96% (98.6% in the specific case of pituitary tumors);
  - Nadeem et al. [31] review a large number of network architectures (mostly, CNN) for brain tumor detection and evaluation. The detection/classification phase reports values of the accuracy in the range 83-98.5%.
- Concerning the segmentation phase:
  - Bhandari et al. [6] compare various approaches of CNN-type applied to the segmentation of glioblastomas in MR images. Most of the algorithms considered obtain a *DSC* in the range 0.85 to 0.92 for the whole tumor;
  - Similar quality scores are reported by Nadeem et al. [31] in the review of segmentation algorithms.
  - Bernal et al. [5] perform a more complex comparison, in particular using overlapping in the training phase, and 3D algorithms as a more complex and accurate alternative to 2D ones. Except for a clear advantage from both these tools, performances reported for the various methods are still in a similar range.

It might be inferred therefore that, in a loose comparison with other established techniques (mostly based on pure neural networks), the processing pipeline under consideration provides a comparable (in many cases, better) quality, despite the relatively light training.

6. Conclusions and future work

In this paper, a technique for fully automatic segmentation of tumors in MRI images has been developed, by integrating three fundamental steps: an anisotropic image filter as a pre-processing step, a deep convolutional neural network for tumor detection and a level set active contour model for the final segmentation.

Each of these three steps might be considered as partly independent from the others, and accomplished with different specific recipes; a careful coupling of the various recipes, however, turns out to be essential for the final success. The major contribution of this paper is to devise a combination leading to remarkably good performances: Perona–Malik filter for pre-processing, a detection neural network combining a pre-trained classification CNN (ResNet-18) and the Faster-RCNN detector, and, finally, an expanding eikonal-type level set active contour model for segmentation. This procedure proved successful in automating the segmentation of meningiomas in T1-weighted contrast enhanced MRI images with reasonably high accuracy. A further advantage of this technique is to require a relatively light training by exploiting the potential of the transfer learning approach.

On the other hand, a critical step is the initialization of the contour for segmentation, which heavily affects the accuracy of the processing chain; the extension to other types of images and tumors might require a careful consideration of the shape and structure of the tumors to be detected and segmented.

Future work on the subject will be directed towards other issues which are attracting attention in this field of research:

- An extension of the algorithm with a further classification among malignant and benign tumors, as well as of the type of the brain tumor (e.g., glioma, glioblastoma,...);
- A three-dimensional version of the algorithm, which could allow to track other relevant parameters of the tumor, such as volume changes in time.

Human and animal rights

The authors declare that the work described has not involved experimentation on humans or animals.

Informed consent and patient details

The authors declare that this report does not contain any personal information that could lead to the identification of the patient(s) and/or volunteers.

Funding

This work has been supported by the GNCS INdAM project "Numerical methods for imaging: from 2D to 3D" and by SBAI–"Sapienza" University of Rome.

Author contributions

All authors attest that they meet the current International Committee of Medical Journal Editors (ICMJE) criteria for Authorship.

Declaration of competing interest

The authors declare that they have no known competing financial or personal relationships that could be viewed as influencing the work reported in this paper.

References

[1] R. Adams, L. Bischof, Seeded region growing, IEEE Trans. Pattern Anal. Mach. Intell. 16 (1994) 641–647.

[2] M.E. Aidouni, Evaluating object detection models: guide to performance metrics, https://manalelaidouni.github.io/manalelaidouni.github.io/Evaluating-Object-Detection-Models-Guide-to-Performance-Metrics.html, 2019.

[3] E. Angelini, Y. Jin, A. Laine, State of the art of level set methods in segmentation and registration of medical imaging modalities, in: Handbook of Biomedical Image Analysis, 2005, pp. 47–101.

[4] L. Barghout, J. Sheynin, Real-world scene perception and perceptual organization: lessons from computer vision, J. Vis. 13 (2013) 709.

[5] J. Bernal, K. Kushibar, M. Cabezas, S. Valverde, A. Oliver, X. Lladó, Quantitative analysis of patch-based fully convolutional neural networks for tissue segmentation on brain magnetic resonance imaging, IEEE Access 7 (2019) 89986–90002.

[6] A. Bhandari, J. Koppen, M. Agzarian, Convolutional neural networks for brain tumour segmentation, Insights Imaging 11 (2020) 1–9.

[7] J. Canny, A computational approach to edge detection, IEEE Trans. Pattern Anal. Mach. Intell. 6 (1986) 679–698.

[8] I. Capuzzo-Dolcetta, R. Ferretti, Optimal stopping time formulation of adaptive image filtering, Appl. Math. Optim. 43 (2001) 245–258.

[9] V. Caselles, R. Kimmel, G. Sapiro, Geodesic active contours, in: Proceedings of IEEE International Conference on Computer Vision, IEEE, 1995, pp. 694–699.

[10] K.H. Cha, L. Hadjiiski, R.K. Samala, H.P. Chan, E.M. Caoili, R.H. Cohan, Urinary bladder segmentation in ct urography using deep-learning convolutional neural network and level sets, Med. Phys. 43 (2016) 1882–1896.

[11] T.F. Chan, L.A. Vese, Active contours without edges, IEEE Trans. Image Process. 10 (2001) 266–277.

[12] A. Chattopadhyay, M. Maitra, MRI-based brain tumour image detection using CNN based deep learning method, Neurosci. Inform. 2 (2022) 100060.

[13] J. Cheng, Brain tumor dataset, https://figshare.com/articles/dataset/brain_tumor_dataset/1512427, 2017.

[14] W.R. Crum, O. Camara, D.L. Hill, Generalized overlap measures for evaluation and validation in medical image analysis, IEEE Trans. Med. Imaging 25 (2006) 1451–1461.

[15] G. Gerig, O. Kubler, R. Kikinis, F.A. Jolesz, Nonlinear anisotropic filtering of mri data, IEEE Trans. Med. Imaging 11 (1992) 221–232.

[16] C.A. Glasbey, An analysis of histogram-based thresholding algorithms, CVGIP, Graph. Models Image Process. 55 (1993) 532–537.

[17] L. Grady, E.L. Schwartz, Isoperimetric graph partitioning for image segmentation, IEEE Trans. Pattern Anal. Mach. Intell. 28 (2006) 469–475.

[18] Y. Guo, Y. Liu, T. Georgiou, M.S. Lew, A review of semantic segmentation using deep neural networks, Int. J. Multimed. Inf. Retr. 7 (2018) 87–93.

[19] R. Hashemzehi, S.J.S. Mahdavi, M. Kheirabadi, S.R. Kamel, Detection of brain tumors from mri images base on deep learning using hybrid model cnn and nade, Biocybern. Biomed. Eng. 40 (2020) 1225–1232.

[20] K. He, X. Zhang, S. Ren, J. Sun, Deep residual learning for image recognition, in: Proceedings of the IEEE Conference on Computer Vision and Pattern Recognition, 2016, pp. 770–778.

[21] L. He, Z. Peng, B. Everding, X. Wang, C.Y. Han, K.L. Weiss, W.G. Wee, A comparative study of deformable contour methods on medical image segmentation, Image Vis. Comput. 26 (2008) 141–163.

[22] J. Hui, Object detection: speed and accuracy comparison (Faster R-CNN, R-FCN, SSD, FPN, RetinaNet and YOLOv3), https://jonathan-hui.medium.com/object-detection-speed-and-accuracy-comparison-faster-r-cnn-r-fcn-ssd-and-yolo-5425656ae359, 2018.

[23] ImageNet, Imagenet large scale visual recognition challenge, http://www.image-net.org/challenges/LSVRC/index.html, 2012.

[24] M. Kass, A. Witkin, D. Terzopoulos, Snakes: active contour models, Int. J. Comput. Vis. 1 (1988) 321–331.

[25] S. Kichenassamy, The Perona–Malik paradox, SIAM J. Appl. Math. 57 (1997) 1328–1342.

[26] A. Kristiadi, et al., Deep convolutional level set method for image segmentation, J. ICT Res. Appl. 11 (2017) 284–298.

[27] A. Krizhevsky, I. Sutskever, G.E. Hinton, Imagenet classification with deep convolutional neural networks, Adv. Neural Inf. Process. Syst. 25 (2012) 1097–1105.

[28] S.U. Lee, S.Y. Chung, R.H. Park, A comparative performance study of several global thresholding techniques for segmentation, Comput. Vis. Graph. Image Process. 52 (1990) 171–190.

[29] W. Liu, D. Anguelov, D. Erhan, C. Szegedy, S. Reed, C.Y. Fu, A.C. Berg, Ssd: single shot multibox detector, in: European Conference on Computer Vision, Springer, 2016, pp. 21–37.

[30] S. Ma, Y. Huang, X. Che, R. Gu, Faster rcnn-based detection of cervical spinal cord injury and disc degeneration, J. Appl. Clin. Med. Phys. 21 (2020) 235–243.

[31] M.W. Nadeem, M.A.A. Ghamdi, M. Hussain, M.A. Khan, K.M. Khan, S.H. Almotiri, S.A. Butt, Brain tumor analysis empowered with deep learning: a review, taxonomy, and future challenges, Brain Sci. 10 (2020) 118.

[32] T.A. Ngo, G. Carneiro, Left ventricle segmentation from cardiac mri combining level set methods with deep belief networks, in: 2013 IEEE International Conference on Image Processing, IEEE, 2013, pp. 695–699.

[33] R. Ohlander, K. Price, D.R. Reddy, Picture segmentation using a recursive region splitting method, Comput. Graph. Image Process. 8 (1978) 313–333.

[34] S. Osher, R.P. Fedkiw, Level Set Methods and Dynamic Implicit Surfaces, vol. 153, Springer, 2003.

[35] S. Osher, J.A. Sethian, Fronts propagating with curvature-dependent speed: algorithms based on Hamilton-Jacobi formulations, J. Comput. Phys. 79 (1988) 12–49.

[36] P. Perona, J. Malik, Scale-space and edge detection using anisotropic diffusion, IEEE Trans. Pattern Anal. Mach. Intell. 12 (1990) 629–639.

[37] G. Praveenkumar, R. Nagaraj, Regularized anisotropic filtered tanimoto indexive deep multilayer perceptive neural network learning for effective image classification, Neurosci. Inform. 2 (2022) 100063.

[38] P. Qin, J. Zhang, J. Zeng, H. Liu, Y. Cui, A framework combining dnn and level-set method to segment brain tumor in multi-modalities mr image, Soft Comput. 23 (2019) 9237–9251.

[39] J. Redmon, S. Divvala, R. Girshick, A. Farhadi, You only look once: unified, real-time object detection, in: Proceedings of the IEEE Conference on Computer Vision and Pattern Recognition, 2016, pp. 779–788.

[40] A. Rehman, M.A. Khan, T. Saba, Z. Mehmood, U. Tariq, N. Ayesha, Microscopic brain tumor detection and classification using 3d cnn and feature selection architecture, Microsc. Res. Tech. 84 (2021) 133–149.

[41] F. Rehman, S.I.A. Shah, M.N. Riaz, S.O. Gilani, R. Faiza, A region-based deep level set formulation for vertebral bone segmentation of osteoporotic fractures, J. Digit. Imaging 33 (2020) 191–203.

[42] S. Ren, K. He, R. Girshick, J. Sun, Faster r-cnn: towards real-time object detection with region proposal networks, arXiv preprint, arXiv:1506.01497, 2015.

[43] O. Ronneberger, P. Fischer, T. Brox, U-net: convolutional networks for biomedical image segmentation, in: International Conference on Medical Image Computing and Computer-Assisted Intervention, Springer, 2015, pp. 234–241.

[44] A. Sachan, Zero to hero: guide to object detection using deep learning: Faster r-cnn,yolo,ssd, https://cv-tricks.com/object-detection/faster-r-cnn-yolo-ssd/, 2017.

[45] J.A. Sethian, Level Set Methods and Fast Marching Methods: Evolving Interfaces in Computational Geometry Fluid Mechanics, Computer Vision, and Materials Science, vol. 3, Cambridge University Press, 1999.

[46] K. Simonyan, A. Zisserman, Very deep convolutional networks for large-scale image recognition, arXiv preprint, arXiv:1409.1556, 2014.

[47] C. Szegedy, S. Ioffe, V. Vanhoucke, A. Alemi, Inception-v4, inception-resnet and the impact of residual connections on learning, in: Proceedings of the AAAI Conference on Artificial Intelligence, 2017.

[48] C. Szegedy, W. Liu, Y. Jia, P. Sermanet, S. Reed, D. Anguelov, D. Erhan, V. Vanhoucke, A. Rabinovich, Going deeper with convolutions, in: Proceedings of the IEEE Conference on Computer Vision and Pattern Recognition, 2015, pp. 1–9.

[49] M. Tang, S. Valipour, Z. Zhang, D. Cobzas, M. Jagersand, A deep level set method for image segmentation, in: Deep Learning in Medical Image Analysis and Multimodal Learning for Clinical Decision Support, Springer, 2017, pp. 126–134.

[50] WHO Classification of Tumours Editorial Board, World Health Organization Classification of Tumours of the Central Nervous System, International Agency for Research on Cancer, 2021.

[51] Z. Zhang, Y. Wang, J. Zhang, X. Mu, Comparison of multiple feature extractors on faster rcnn for breast tumor detection, in: 2019 8th International Symposium on Next Generation Electronics (ISNE), IEEE, 2019, pp. 1–4.

[52] H.K. Zhao, T. Chan, B. Merriman, S. Osher, A variational level set approach to multiphase motion, J. Comput. Phys. 127 (1996) 179–195.